PAPER

Check for updates

Sonocrystallization induced thermally activated delayed fluorescence *via* distortion of molecular geometry†

Antonio Maggiore, [ID] *[ab] Yangyang Qu,[a] Piotr Pander, [ID] [cd] Fernando B. Dias, [ID] [e] Gilles Clavier, [ID] [a] Regis Guillot, [ID] [f] Davide Altamura,[g] Cinzia Giannini,[g] Vincenzo Maiorano,[b] Pierre Audebert [ID] [a] and Fabien Miomandre[a]

In this work, we present three donor–acceptor thermally activated delayed fluorescence (TADF) molecules comprising a 2,3,5,6-tetrafluorobenzonitrile acceptor with various electron donor units: phenoxazine (**Phx-BzN**), phenothiazine (**Pht-BzN**), and carbazole (**Cz-BzN**). These molecules have been studied using steady-state and time-resolved photophysical techniques in solution, film in polymer host and in crystal state. While **Cz-BzN** displays TADF in solution and polymethyl methacrylate (PMMA) films, **Phx-BzN** and **Pht-BzN** are non-emissive in solution and somewhat emissive in polymer films. More interestingly, while **Pht-BzN** remains virtually non-emissive in all studied solvents, it exhibits strong photoluminescence and TADF in crystal state, attributed to Crystallization Induced Emission (CIE). Interestingly, by applying ultrasound to an amorphous **Pht-BzN** water suspension we were also able to induce a reorganization of the molecules obtaining a microcrystal suspension. This can represents a new strategy to develop luminescent organic microcrystalline materials. We demonstrate through computational studies that the CIE properties arise due to intermolecular interactions in the crystal structure that result in locking the ground state molecular geometry and blocking relaxation in the excited state. As a result, the oscillator strength in the crystal form is enhanced leading to a highly luminescent behaviour, while in solution it equals nearly zero due to the molecule adopting a perfectly orthogonal D–A orientation in the excited state.

Introduction

Efficient luminescent organic materials that present thermally activated delayed fluorescence (TADF) have recently attracted enormous attention due to effectively harvesting triplet excited states without using heavy metals – a property desired for application in organic light-emitting diodes (OLEDs). The most common strategy to achieve TADF in organic molecules is by using donor–acceptor (D–A) systems presenting a near ortho-gonal orientation between the D and A units. This allows to reduce the overlap of the HOMO and LUMO and thus to obtain a very small energy gap between singlet and triplet excited states (ΔE_{ST}).[1–6] Nevertheless, these emitters are bound by a trade-off between the singlet radiative rate and HOMO–LUMO overlap: the latter must be suitably small to achieve $\Delta E_{ST} \approx 0$ but large enough to retain high photoluminescence quantum yield (PLQY). For this reason, various strategies have been proposed to achieve the best compromise between these two factors.[2,4,5,7,8] These organic, π-conjugated materials exhibit luminescent properties that can be tuned by a change in their structure[9] (*e.g.* through donor and acceptor strength or bulky groups introducing steric hindrance) or by changing the sur-rounding environment or matrix (*e.g.* polarity and rigidity of the medium) where the molecule is dispersed. This feature allows controlling the emission nature by tuning the energy of the electronic states involved in the TADF process and thus also tuning the triplet excited state harvesting mechanism.

Most fluorescent dyes require low concentration in solution or in solid matrix conditions to suppress aggregation caused quenching (ACQ). ACQ is a common phenomenon which

[a] *Université Paris-Saclay, ENS Paris-Saclay, CNRS, PPSM, Gif-sur-Yvette, 91190, France. E-mail: antonio.maggiore@nanotec.cnr.it*

[b] *CNR-NANOTEC – Institute of Nanotechnology, c/o Campus Ecoteckne, Via Monter-oni, 73100 Lecce, Italy*

[c] *Faculty of Chemistry, Silesian University of Technology, Strzody 9, 44-100 Gliwice, Poland*

[d] *Centre for Organic and Nanohybrid Electronics, Silesian University of Technology, Konarskiego 22B, 44-100 Gliwice, Poland*

[e] *Department of Physics, University of Durham, South Road, Durham, DH1 3LE, UK*

[f] *CNRS, Institut de chimie moléculaire et des matériaux d'Orsay, Université Paris-Saclay, Orsay, 91405, France*

[g] *Institute of Crystallography CNR-IC, Via Amendola 122/O, Bari 70126, Italy*

† Electronic supplementary information (ESI) available. CCDC 2243330 and 2243331. For ESI and crystallographic data in CIF or other electronic format see DOI: https://doi.org/10.1039/d4tc00245h

This journal is © The Royal Society of Chemistry 2024

J. Mater. Chem. C, 2024, **12**, 7943–7955 | 7943

seriously affects luminescence in solution at high concentrations, and in powder or neat film form, leading to low PLQY or complete emission quenching in these conditions. ACQ is caused by formation of aggregated species such as dimers, excimers and H-aggregates *via* strong intermolecular π–π interactions – it occurs especially for flat and highly conjugated molecules.[10,11] In contrast with ACQ, aggregation induced emission (AIE) leads to a significant increase of PLQY in solid forms of the emitter, such as in neat film or crystal.[12–14] AIE materials display negligible PLQY in solution due to vibrational quenching of their electronic excited states. Therefore, AIE relies on restricting intramolecular roto-vibrational motions in solid state by means of physical stacking that prevents strong π–π interactions and efficiently blocks exciton quenching channels, mode generally favoured in molecules with a propeller-like structure.[15,16] Crystallization induced emission (CIE) is a similar phenomenon to AIE, but occurring in crystals.

Organic crystals display long-range ordering, high chemical purity, optical emission enhancement, wave-guiding, and high stability[17–20] which renders them attractive for applications in solid-state optoelectronic devices, such as light-emitting transistors, photovoltaics, and OLEDs. AIE/CIE molecules may be used for visualization of chemical and biological processes in the nanoscale.[21–24] A large number of AIE molecules have also been used as smart materials responsive to fluorescence, chemo- and colorimetric sensing,[25,26] as sensors or probes for selective detection of specific biological tissues[27–29] such as cancer cells,[30] and also for singlet oxygen generation in photodynamic therapy.[31] Most recent advances and developments in the area of AIE materials originate from important advantages presented by these systems, *e.g.* non-invasiveness, simplicity, high spatio-temporal resolution and sensitivity.[32]

Emitters that simultaneously display TADF and AIE are known as aggregation-induced delayed fluorescence (AIDF) emitters. Interestingly, the usual design feature of D–A TADF luminophores: the D and A units twisted in respect to each other, helps preventing the strong π–π interactions that would lead to ACQ.[33] TADF emitters are thus promising for use in highly-emissive neat films such as host-free OLEDs.[34,35] The first AIDF donor–acceptor compound was reported by Wang and others in 2014.[36] The authors demonstrated that weak intermolecular non-covalent interactions in the solid state, such as C–H···π, are fundamental to suppress intramolecular rotations that lead to excited state quenching, thus turning emission on. AIDF-active luminophores have also been studied as emitters in non-doped OLEDs.[37–45]

In this work, we present a photophysical study of three different D–A TADF emitters (Fig. 1) with a 2,3,5,6-tetrafluorobenzonitrile acceptor unit (we will call it fluorobenzonitrile or BzN from now on) substituted in the *para* position to the –CN group with various donors: carbazole (**Cz-BzN**), phenoxazine (**Phx-BzN**), and phenothiazine (**Pht-BzN**). The synthesis of **Cz-BzN** and **Pht-BzN** follows the methodology reported previously for the **Phx-BzN** derivative.[46] Synthetic details are presented in the ESI.† The nature of the donor and acceptor moieties has a profound impact on their TADF properties.[2,47] In this work we
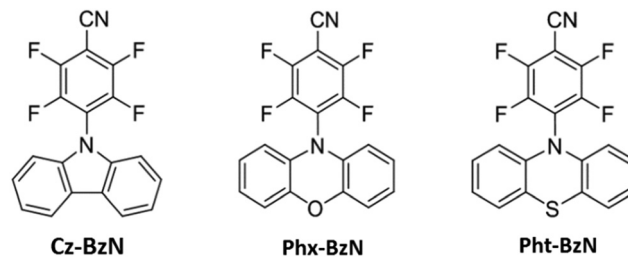

Fig. 1 Structures of molecules studied in this work.

demonstrate a completely new mechanism that allows activating both luminescence and TADF through a tailored molecular arrangement in crystal lattice. We believe this to be a significant advancement over the currently known examples of TADF AIE/CIE materials.[48] Furthermore, this work serves as a proof-of-concept for a new simple one-step method for producing luminescent microcrystals through use of sonication.

Great efforts have been undertaken in the last decades to develop nanotechnology-based materials for use in different areas of research, such as: chemistry,[49] physics,[50] engineering,[51] biology and medical sciences.[52,53] Our study demonstrates a new versatile and powerful strategy for developing fluorescent organic nanoparticles and microcrystals and contributes to a further advancement in developing functional nanomaterials. In particular, our self-assembly material **Pht-BzN** could find application in high-performance optoelectronic devices, biological sensing and imaging, discrimination and bioimaging.

Results and discussion

X-Ray diffraction analysis (XRD)

The geometrical structures of the three molecules were obtained with X-ray scattering analysis (Fig. S1–S3 and Fig. 2 top, ESI†). The structural properties play a crucial role in the understanding of the photophysical properties of the materials reported in this work. A summary of key angles identified in the single crystal structures is shown in the ESI,† Table S2. Notably, two molecules are present in the crystal unit cell of **Pht-BzN**, each of them with a slightly different configuration (we will use terms *molecule 1* and *molecule 2* to distinguish them). It can be noted that the D–A dihedral angle increases from 50.70° in **Cz-BzN**, to 83.31° in **Phx-BzN**, and further to 89.22° (*molecule 1*) and 86.11° (*molecule 2*) in **Pht-BzN** (Table S2, ESI†). As in **Cz-BzN** the D–A angle is relatively small we can expect a degree of conjugation between carbazole and the BzN. Contrariwise, **Phx-BzN** and **Pht-BzN** with stronger donors show large D–A dihedral angles indicating near-orthogonality between donor and acceptor moieties. The molecular crystal packing shown in Fig. 2 bottom and in Fig. S4–S7 (ESI†) reveals the main molecular interactions that play a key role in the formation of the crystal structure. In **Cz-BzN** single crystal the main intermolecular interactions are: C–H···π (3.238 –3.480 Å), C–N···π (3.516 Å) C–N···H (2.552 Å) and C–F···H (2.553 Å), while in **Phx-BzN** crystal the main intermolecular interactions are: C–H···π (2.847 Å), C–F···π (3.166 Å), C–F···H (2.634 Å, 2.499 Å) and

7944 | *J. Mater. Chem. C*, 2024, **12**, 7943–7955

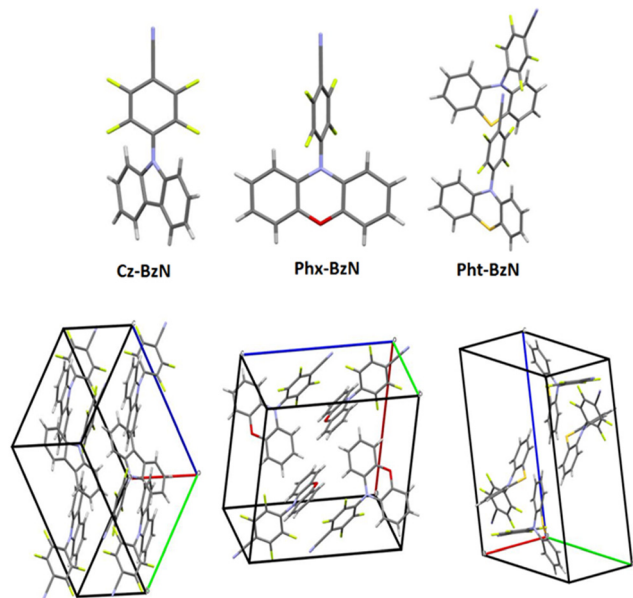This journal is © The Royal Society of Chemistry 2024

Fig. 2 Top: X-ray crystallographic structures of, from left to right, **Cz-BzN**, **Phx-BzN**, **Pht-BzN**. Bottom: Molecular packing of, from left to right, **Cz-BzN**, **Phx-BzN**, **Pht-BzN** obtained from X-ray crystallographic structures.

Fig. 3 Optimized structures of, from left to right: **Cz-BzN**, **Phx-BzN** and **Pht-BzN**. (Bottom) Ground state (S_0); (top) lowest singlet excited state (S_1).

O···H (2.563 Å) (Fig. S6, ESI†). Finally, in **Pht-BzN** crystal the main intermolecular interactions are: C–F···π (3.072 Å), C–F···H (3.025 Å), C–H···π (3.004 Å) and C–N···H (2.656 Å) (Fig. S7, ESI†). From these analyses, we conclude that no π–π stacking occurs, thus luminescence properties in crystal are solely of intra-molecular origin.

Density functional theory (DFT) calculations

The molecules were studied using density functional theory (DFT) and time-dependent density functional theory (TD-DFT) to help interpreting the subsequent experimental photophysical data. Details on theoretical calculations can be found in Section 3.3 of the ESI.† Simulated ground state (S_0) structures (Fig. 3 bottom) match relatively well the experimental XRD structures (Fig. S11, Table 1 and Table S2, ESI†) indicating the level of theory used is adequate to represent the real systems. The calculated geometries of the BzN acceptor fragments are planar in all cases. In the case of **Cz-BzN** and **Phx-BzN** the carbazole and phenoxazine donors are close to planarity but not perfectly flat (Table 1). However, in **Pht-BzN** the phenothiazine N and S atoms adopt an off-planar configuration leading to deformation of the planar donor geometry (angle D = 31.6° in Table 1). As a result, the donor and the acceptor in **Pht-BzN** are quasi-axial (see D–A angle in Table 1) as previously shown in similar compounds.[54,55] The HOMO is localised mostly on the donors, while the LUMO is mostly located on the acceptor BzN unit. The localization of HOMO on the donor is more pronounced for molecules with stronger donors: **Phx-BzN** and **Pht-BzN** than in **Cz-BzN** (Fig. 4). In **Cz-BzN** the HOMO is localized on the donor moiety but with a small contribution from the benzonitrile unit, while this effect is negligible in **Phx-**
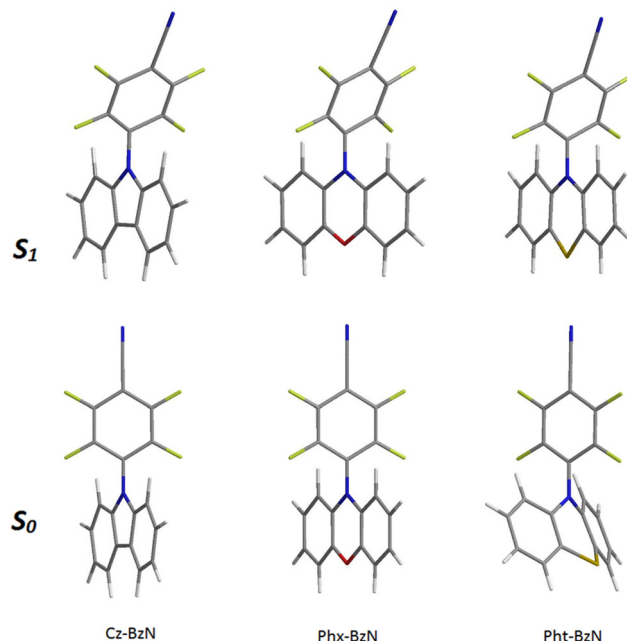
BzN and **Pht-BzN**. A similar general trend applies to the LUMO with a partial contribution of donor to the orbital evident for **Cz-BzN**, but also for **Phx-BzN** (Fig. 4). The results confirm that a partial D–A conjugation exists for **Cz-BzN**.

TD-DFT calculations reveal that the energetically lowest singlet transition ($S_1 \rightarrow S_0$) corresponds to an ICT state for the ground state (S_0), first singlet excited (S_1) and first triplet (T_1) geometries (Table S7, ESI†). The oscillator strength of this transition decreases in the series for all three geometries. In particular, for the ground state geometry we observe: **Cz-BzN** (0.2155) > **Phx-BzN** (0.052) > **Pht-BzN** (0.0006) (Table S7, ESI†). The change in oscillator strength correlates with the D–A angle in the ground state (S_0) geometry (Table 1). It is evident that as the D–A angle approaches 90°, the HOMO and LUMO become more orthogonal. Consequently, their overlap decreases, reducing communication between them and directly affecting the oscillator strength of this electronic transition. Reduced oscillator strength of the $S_1 \rightarrow S_0$ transition often leads to lowering photoluminescent properties of the luminophores, despite simultaneously reducing the ΔE_{ST}. The second lowest singlet state (S_2) corresponds to a π–π* localized transition centred at the donor (locally excited state, ^{1}LE, Table S7, ESI†). Generally speaking, higher energy transitions have a π–π* ^{1}LE character and are centred on either of the D or A moieties.

The S_1 geometries are shown in Fig. 3 top, while key angles relevant to the computed structures are shown in Table 1. We observe a rather large reorganization through twisting of the benzonitrile unit relative to the donor (Fig. S10, ESI†), and thus a large Stokes shift between absorption and emission can be expected. Donors fully planarize in the S_1 geometry, which is more evident for **Pht-BzN**, while the D–A become fully or near fully orthogonal. The corresponding MOs become more

This journal is © The Royal Society of Chemistry 2024

J. Mater. Chem. C, 2024, **12**, 7943–7955 | 7945

Table 1 Calculated key angles for the ground (S_0) and excited state structures

	S_0				S_1				T_1		
	D^a (°)	D–A (°) dihedral angle		$D–A^b$ (°)	D^a (°)	D–A (°) dihedral angle		$D–A^b$ (°)	D^a (°)	D–A (°) dihedral angle	$D–A^b$ (°)
Cz-BzN	0.4	59.4		59.9	0.0	71.2		90.0	1.6	39.7	57.1
Phx-BzN	1.2	73.5		73.6	0.0	73.3		90.0	5.6	53.4	69.6
Pht-BzN	31.6	85.6		89.8	0.1	75.4		90.0	10.3	57.5	69.0

^{a} D angle refers to the calculated angle between the mean planes of the two phenyl rings of the donor. ^{b} D–A angle refers to the calculated angle between the mean planes of the donor and the acceptor.
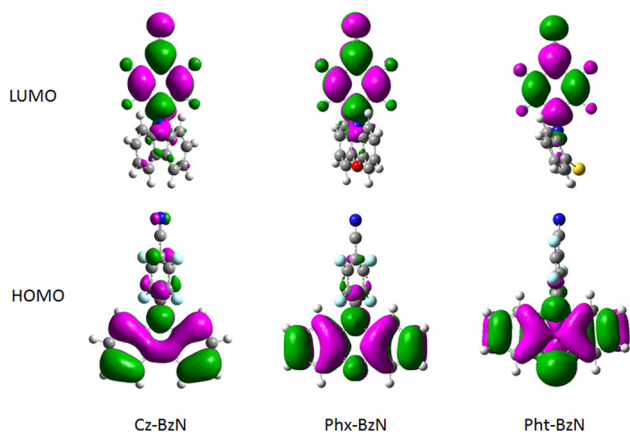
Fig. 4 HOMO and LUMO iso surfaces at the S_0 geometry.

localized on the donor and acceptor units (Fig. S13, ESI†) indicating a more pronounced CT character in the S_1 state, compared with the S_0 geometry (Fig. 4). In **Pht-BzN** and **Phx-BzN** the donor and acceptor are orthogonal at the S_1 geometry and as the MOs are fully localized on each respective moiety, this results in a pure CT nature of the S_1 state leading to the $S_1 \rightarrow S_0$ transition having zero oscillator strength (Table S6, ESI†).

We observe a slight difference in the T_1 geometry of **Cz-BzN** but for **Phx-BzN** and **Pht-BzN** the T_1 geometry is very similar to that in the S_1 state (Fig. S10, ESI†). This has an impact on the energy levels of the excited singlet and triplet states (Fig. S19, ESI†): for **Phx-BzN** and **Pht-BzN** the T_1 and S_1 levels remain close at both T_1 and S_1 geometries while for **Cz-BzN** we observe an increased ΔE_{ST} value.

At all three considered geometries the T_1 displays a ^3CT nature, while the T_2 is of local (donor or acceptor) ^3LE character (Fig. S19 and Table S7, ESI†). Notably, the ^3LE is close in energy to the ^3CT in the S_0 geometry for all three molecules, while these states are around 1 eV away from each other in the T_1 geometry. At S_1 geometries, the ^3LE and ^3CT states in **Cz-BzN** are close in energy, while in **Phx-BzN** and **Pht-BzN** they are, again, ∼1 eV away from each other. Given that the most efficient RISC occurs with a closely located triplet mediator state of different orbital geometry from the S_1, we can conclude that more favourable conditions for TADF are present in the S_0 geometry rather than in the excited state.[56]

In conclusion, **Phx-BzN** and **Pht-BzN** are expected to be non-emissive as the pure CT character of their S_1 states leads to a symmetry-forbidden transition. For **Cz-BzN** the oscillator strength is above zero, hence the molecule is predicted to remain luminescent. However, we can expect a different behaviour if the molecules are locked in the S_0 configuration. A smaller D–A angle in this case increases the HOMO–LUMO overlap and decreases the CT character. As a result, **Cz-BzN** is expected to have a large $\Delta E_{ST} = 0.49$ eV, thus TADF is not expected at the S_0 geometry. However, **Phx-BzN** and **Pht-BzN** display small deviation from a full orthogonality at the S_0 geometry, hence the oscillator strength remains above zero in both cases, while ΔE_{ST} is small, <0.15 eV, thus TADF may be present.

Photophysical study

Photophysical properties of the three presented molecules were studied in diluted solution (10^{-6}–10^{-5}M) in three solvents with
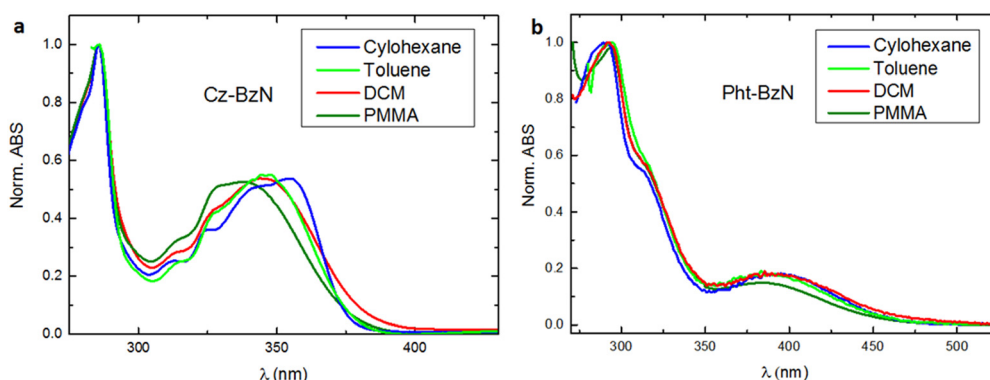

Fig. 5 Normalized absorption spectra of (a) **Cz-BzN** and (b) **Pht-BzN** in cyclohexane, toluene, dichloromethane, and PMMA (0.05 wt%). $c = 10^{-5}$ M in solution.

7946 | *J. Mater. Chem. C*, 2024, **12**, 7943–7955

This journal is © The Royal Society of Chemistry 2024

increasing polarity: cyclohexane (CH), toluene (TOL), and dichloromethane (DCM). To study the intrinsic properties of molecules avoiding intermolecular interactions, the compounds were dispersed in a rigid polymer matrix (PMMA) at very low concentration of only 0.05 wt% Photophysical properties of bulk compounds were studied in crystalline powders. The photophysical properties of **Phx-BzN** in solution and PMMA have been reported previously and are not discussed in detail in this work.[46]

Photophysical properties in solution

The UV-Vis absorption spectra of **Cz-BzN** and **Pht-BzN** are shown in Fig. 5. One may note a weak band extending out until 400 nm in **Cz-BzN** and 450–500 nm in **Pht-BzN**. Using TD-DFT this band can be assigned to a CT HOMO → LUMO transition between donor and acceptor. In particular, for **Cz-BzN** we can observe a clear bathochromic shift of the onset with the increasing solvent polarity, which confirms its CT nature. On the other hand, with the increasing of solvent polarity we can also note a change on the shape of this band, *i.e.* the vibronic resolution decreases indicating its hybrid local and charge transfer (HLCT) character. In **Pht-BzN** the transition at lower energy appears much less intense relatively to the **Cz-BzN**. This band exhibits a slight bathochromic shift in DCM, as usually for CT transitions. On the other hand, the absorption bands at higher energy do not shift with polarity and can be assigned to local absorption of carbazole[57,58] in **Cz-BzN** (bands at λ_{max} = 325–330 nm and λ_{max} = 286 nm) and phenothiazine[59] in **Pht-BzN** (band at λ_{max} = 290 and the shoulder at 315 nm).

Steady-state photoluminescence spectra of **Cz-BzN** and **Pht-BzN** in solution are shown in Fig. 6. All presented molecules are characterized by the formation of an intramolecular charge-transfer state, but may display luminescence from both: LE and CT states.[60,61] In solution, only **Cz-BzN** displays intense photoluminescence, while **Pht-BzN** remains non-emissive in all solvents except in cyclohexane (Fig. 6a) where only a very weak emission of near negligible intensity (PLQY = 0.2%) is observed. The emission intensity also remains invariant of the presence of oxygen, indicating no significant contribution from TADF. The more luminescent **Cz-BzN** shows a clear positive solvatochromism (Fig. 6b). Such behaviour confirms the CT character of the emissive excited state.[62] Among the three solvents used in the study, **Cz-BzN** displays the highest PLQY in toluene and cyclohexane (Table 2). The PLQY remains lower in DCM due to the strongly stabilised CT and thus stronger effect of non-radiative processes.[63–66]

The luminescence decay lifetimes of **Cz-BzN** in degassed solutions are shown in Table 2, while the respective decay traces are shown in Fig. 6c and d. We observe two monoexponential decay regimes in all three solvents used in the study. The short decay component in the nanosecond regime can be assigned to prompt fluorescence, while the longer decay component in the microsecond regime can be attributed to TADF.

Steady-state photoluminescence properties in solid *vs.* solution

Photoluminescence spectra in PMMA and in crystalline powder display a broad featureless shape (Fig. 7) and are likely originated from a CT state, as in solution. The emission spectra in
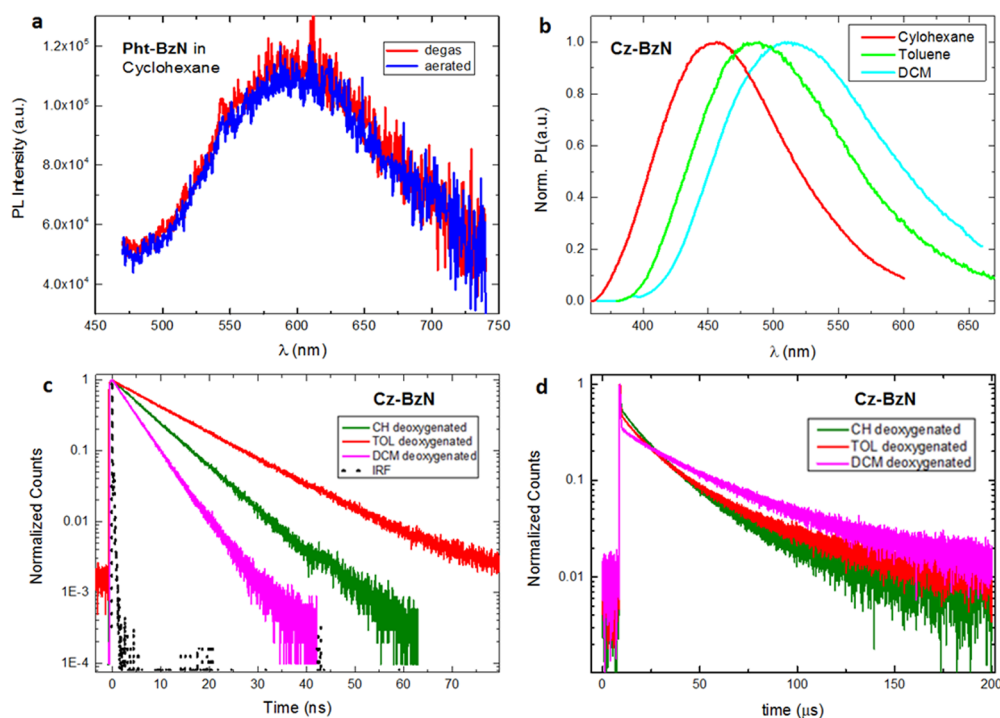

Fig. 6 (a) Photoluminescence spectra of **Pht-BzN** in cyclohexane in aerated and degassed solution. (b) Normalized photoluminescence spectra of **Cz-BzN** in solvents with increasing polarity: cyclohexane, toluene, DCM, and in PMMA, λ_{ex} = 330 nm. (c) Decay curves of **Cz-BzN** in cyclohexane, toluene and DCM in the nanosecond timescale. (d) Decay curves of **Cz-BzN** in cyclohexane, toluene and DCM in the microsecond timescale.
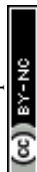
This journal is © The Royal Society of Chemistry 2024

J. Mater. Chem. C, 2024, **12**, 7943–7955 | 7947

Table 2 Summary of photophysical properties in solution

Molecule	Solvent	λ_{Abs} (nm)	λ_{PL} (nm)	FWHM (nm)	PLQY^{air}/PLQY$^{(deoyg)}$ (λ_{exc} = 330 nm)	$\tau_{PF}^{(deoyg)}$ (ns)	$\tau_{DF}^{(deoyg)}$ (µs)
Cz-BzN	CH	286, 312, 324, 341(s), 354	457	115	0.13/0.16	9.0	26.8
	TOL	286, 314(s), 327(s), 346	485	134	0.14/0.18	11.6	35.2
	DCM	286, 314(s), 327(s), 343	511	149	0.06/0.07	4.8	43.6
Pht-BzN	CH	291, 314(s), 395	602	141	0.002/0.002	—	—
	TOL	294, 316(s), 390	n.e.	n.e.	n.e.	n.e.	n.e.
	DCM	293, 313(s), 394	n.e.	n.e.	n.e.	n.e.	n.e.

$^{(deoyg)}$Deoxygenated, $^{(s)}$denotes a shoulder, n.e. non-emissive. Experimental error for PLQY is estimated at ±20%.

PMMA appear blue shifted in respect to cyclohexane for all three compounds (Table 2 and Table S7, see ref. 46 for **Phx-BzN**, ESI†). This blue shift is due to a rigidochromic effect: limiting rotational/vibrational motions of molecules and suppressing geometrical relaxation leads to the excited state configuration being more similar to that of the ground state. Concomitant with the rigidochromic effect is a decrease in the spectrum FWHM and an increase in the PLQY. A similar rigidochromic effect is at play in crystal powders, which leads to even higher PLQY and narrower PL spectra (Tables 2, 3 and Tables S7, S9, see ref. 46 for **Phx-BzN**, ESI†). However, the CT energy does not follow a clear trend, which might be due to solid state solvation affecting the molecular dipole.[67] Considering the solution and solid-state photophysics one may conclude that **Cz-BzN** (Table 3) displays crystallization-induced enhanced emission (CIEE, a phenomenon similar to CIE),[11,68] while **Phx-BzN** (Table S9, ESI†) and **Pht-BzN** (Table 3) display CIE.

By comparing the photoluminescence of the molecules dispersed in PMMA with that in the crystalline powders (Fig. 7) we notice that for **Cz-BzN** (Fig. 7a) the emission spectrum is narrower in the crystal form, but the position of the maximum is the same. This is consistent with suppression of molecular vibrations in **Cz-BzN** crystals. The bathochromic PL shift observed for **Phx-BzN** crystals (Fig. 7b) is related to the increased stabilisation of the CT state by the ground state dipoles of neighbouring molecules.[67] For example, orientation of the molecular dipoles in **Phx-BzN** crystal may lead to a significant stabilisation of the excited CT state. We believe the effect is not due to aggregation as packing in the **Phx-BzN** crystals (Fig. S6, ESI†) does not reveal any π–π stacking. The **Pht-BzN** crystalline powder shows a significant hypsochromic shift in respect to PMMA films (Fig. 7c), and a large increase of

the PLQY to 39% (from only 0.2% in cyclohexane, Table 3), in agreement with our assignment of the CIE properties. We note that **Pht-BzN** is only modestly luminescent in PMMA, PLQY = 1.7% (Table 3), thus we believe the high PLQY in crystal is due to the highly rigid environment.

AIE properties and sonication-induced crystallization

To probe the AIE properties of **Phx-BzN** and **Pht-BzN** we precipitate them from dilute THF solutions by gradually adding water, which yields amorphous colloidal aggregates (see details in the ESI,† Section 1.2). We observe that THF/water mixtures with water fraction f_w < 90% display a very low PL intensity, while upon further rise of water content PL increases significantly, indicative of aggregate formation (Fig. 8 and Fig. S22, ESI†). The dispersion obtained from **Phx-BzN** in THF/water mixture displays an emission profile similar to the crystalline powder (Fig. 7b and Fig. S22, ESI†), but the same is not true for the **Pht-BzN** where we observe a pronounced red shift (λ_{max} = 575 nm) in respect to the crystal PL and a significantly lower PLQY = 1% (Table 3), rather similar to that in amorphous neat film (Fig S21, ESI†). Based on these results we believe that the obtained dispersions are amorphous. Since **Cz-BzN** presents high solution PLQY we did not probe its AIE properties.

To induce crystallization of the amorphous **Pht-BzN** dispersion, the suspension was sonicated for 10 minutes (see details in ESI,† Section 1.2). After sonication the dispersion of **Pht-BzN** (Fig. 8 right) shows a significantly stronger and blue shifted luminescence, PLQY = 22% and λ_{max} = 500 nm. Its PL spectrum closely matches that of the crystal powder, thus we attribute crystalline character to this sonicated dispersion. Grazing incidence wide-angle X-ray scattering (GIWAXS) measurements performed on the solution
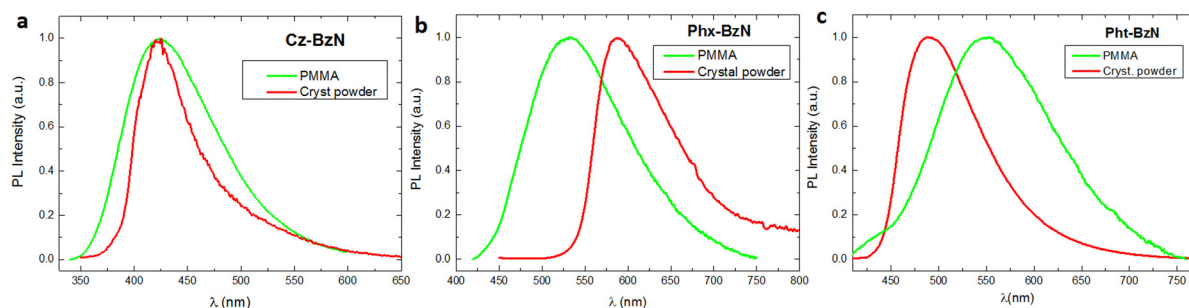

Fig. 7 Normalized steady-state photoluminescence spectra in PMMA films (0.05 wt%) and in crystalline powders for (a) Cz-BzN; (b) Phx-BzN; (c) PhtBzN. λ_{ex} = 330 nm.

7948 | *J. Mater. Chem. C*, 2024, **12**, 7943–7955

This journal is © The Royal Society of Chemistry 2024

Table 3 Photophysical properties of **Cz-BzN** and **Pht-BzN**

Molecule	Form	Temp. (K)	λ_{Abs} (nm)	λ_{PL} (nm)	$\Phi_{PL}/\Phi_{PL}{}^{deox}$	τ_{PF} (ns)	τ_{DF} (μs)	$\tau_{phos.}$ (ms)	$\Delta E_{S-T}{}^{c}$ (eV)	DF/PF^{d}	$k_{ISC}{}^{e}$ (s^{-1})	$k_{RISC}{}^{e}$ (s^{-1})
Cz-BzN	PMMA	295	286, 314(s), 328(s), 338	448	0.30/0.39	8.4	$20.5^{b}/2700^{b}$	—	—	0.09	—	—
	PMMA	80	—	450	$—/0.58^{a}$	9.5	—	—	—	—	—	—
	Crystal	295	—	439	0.46	2.8	—	—	—	—	—	—
	Crystal	80	—	446	$—/1.00^{a}$	3.0	1.6^{b}	—	—	0.05	—	—
Pht-BzN	PMMA	295	293, 313(s), 386	540	0.017/0.021	4.1	1.4^{b}	—	0.09	0.61	—	—
	PMMA	80	—	532	$—/0.105^{a}$	6.9	50.5^{b}	6.70	—	0.31	—	—
	Crystal	295	—	500	$—/0.39^{a}$	8.5	2.3	—	0.02	5.0	9.7×10^{7}	2.6×10^{6}
	Crystal	80	—	488	$—/0.92^{a}$	12	1187	—	0.01	7.3	7.3×10^{7}	7.0×10^{3}
	Nanocryst. dispersion	295	—	502	$—/0.22$	20.6^{b}	2.7^{b}	—	—	3.46	—	—

$^{(deox)}$ oxygen-free conditions, $^{(s)}$denote a shoulder. ^{a} PLQY estimated by comparing the PL intensity at RT with that at 80 K. ^{b} Average decay lifetime from biexponential fit. (Determination of the average decay time is described in ESI Section S1.4.) ^{c} Calculated from the onset of the delayed fluorescence and phosphorescence spectra. ^{d} Delayed fluorescence to prompt fluorescence ratio derived as a ratio of integrated delayed fluorescence (DF) and prompt fluorescence (PF) intensity from the fitted decay curves. ^{e} The rate constant of ISC and RISC (determined by using the method reported in ESI Section S1.4, valid only for DF/PF $\geq$ 4). The experimental error for Φ_{PL} is $\pm20\%$ of the value.
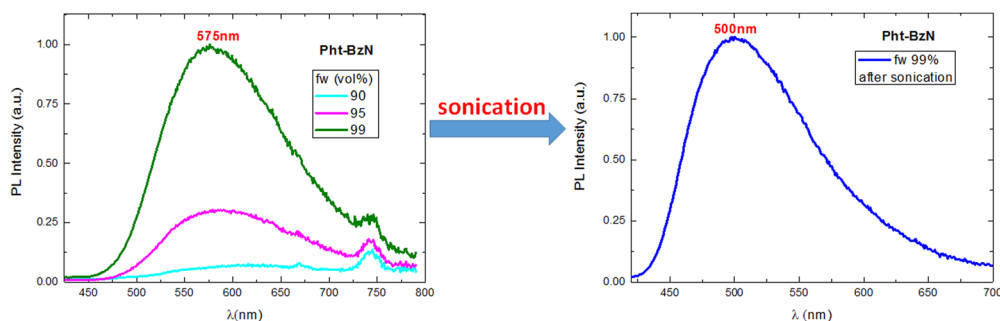

Fig. 8 Left: PL spectra of **Pht-BzN** in THF/water mixtures with varying water fraction (f_w = 90, 95 and 99%), λ_{ex} = 370 nm. Right: PL spectrum of **Pht-BzN** in THF/water after sonication, λ_{ex} = 370 nm.

containing the microcrystals casted onto a silicon substrate revealed clear diffraction signals (Fig. S8, ESI†), confirming the presence of crystals in the suspension (see details in ESI,† Section 3.2). The dimensions of the obtained microcrystals were determined using the DLS technique (see details in ESI,† Section 1.3), which resulted in particle sizes distributed mostly around 250 nm and partially around 650 nm (Fig. S35, ESI†).

Amorphous *vs.* crystalline films

To gain further insight into the properties of **Pht-BzN** in amorphous and crystal states we first studied the molecule in neat film. A pristine film obtained by fast evaporation of a concentrated DCM solution of **Pht-BzN** presents the same emission spectrum as the initial (amorphous) colloidal dispersion described above. However, the film spontaneously crystallizes within an hour at RT (Fig. S21a, ESI†), resulting in significant blue shift and increase in PL intensity of the newly formed phase (Fig. S21b, ESI†). We conclude that the seasoned film should be treated as crystalline as its PL spectrum agrees with that in crystals. We observe an increase of PLQY from 0.5% in amorphous film to 8% in crystalline film. The lower PLQY in the **Pht-BzN** crystalline film compared to crystalline powder strongly suggests the presence of quenchers in the former.

These could be occluded solvent or oxygen from air that are less likely to affect luminescence in larger crystals.

Time-resolved photophysical study in solid state

Time-resolved photoluminescence studies were performed to gain more insight into the nature of the PL behavior of **Cz-BzN** and **Pht-BzN** in solid phase. We focus on these two luminophores in the rest of the main article text. Results relevant to **Phx-BzN** can be found in the ESI,† Section 3.4.3.

Time-resolved photophysical study of Cz-BzN and Pht-BzN in PMMA films. Time-resolved PL spectra of **Cz-BzN** and **Pht-BzN** in PMMA are shown in Fig. 9a, 9c and Fig. S24, S30 (ESI†). The PL traces are characterized by a short decay component in the 2–10 ns timescale which we assign to prompt-fluorescence (PF). PF is followed by a slow PL decay in the microsecond regime that is attributed to TADF. We note that at RT, the PF appears blue shifted in respect to DF in both cases. This behaviour is very common among donor–acceptor systems and can be attributed to a slow geometry relaxation in the excited state or to the occurrence of various metastable excited state geometries in the solid phase.[69,70] The decay of **Cz-BzN** (Fig. 9b) can be fitted with a monoexponential expression in the PF regime (τ = 8.4 ns), while the TADF emission presents a
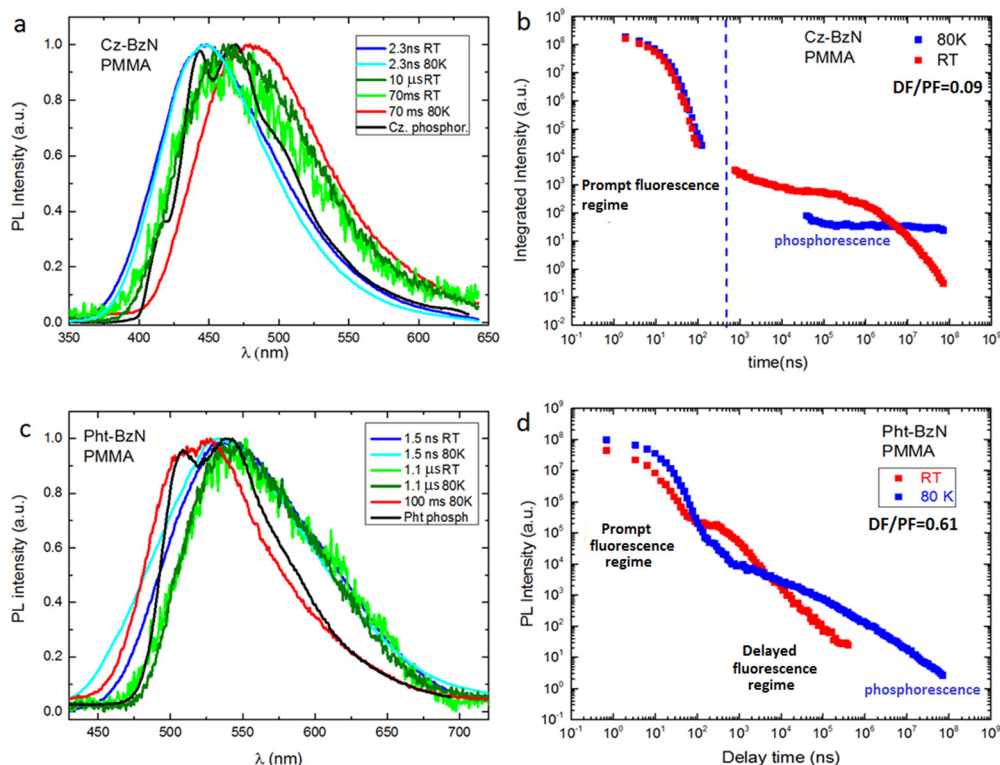
This journal is © The Royal Society of Chemistry 2024

J. Mater. Chem. C, 2024, **12**, 7943–7955 | **7949**

Fig. 9 (a) Time-resolved emission spectra of **Cz-BzN** in PMMA (0.05 wt%) at room temperature and 80 K. Phosphorescence spectrum of carbazole (Cz) at 80 K is indicated with a black line. (b) Photoluminescence decay of **Cz-BzN** in PMMA (0.05 wt%) at RT and 80 K. (c) Time-resolved emission spectra of **Pht-BzN** in PMMA (0.05 wt%) at room temperature and 80 K. Phosphorescence spectrum of phenothiazine (Pht) at 80 K is indicated with a black line. (d) Photoluminescence decay of **Pht-BzN** in PMMA (0.05 wt%) at RT and 80 K. Excitation wavelength: λ_{ex} = 355 nm.

tri-exponential decay with an average decay lifetime of 2.7 ms. The decay trace of **Pht-BzN** at RT (Fig. 9d) is fitted with biexponential expressions in both PF and DF regimes, giving the average lifetime τ_{av} = 4.1 ns for PF and τ_{av} = 1.4 μs for TADF. The relationship between delayed fluorescence intensity and laser excitation dose is linear for both compounds (Fig. S24 and S34, ESI†), a behaviour consistent with TADF. The ratio of delayed to prompt fluorescence (DF/PF) at RT (Table 3) is larger in **Pht-BzN** than in **Cz-BzN**.

Time-resolved PL spectra of **Cz-BzN** and **Pht-BzN** recorded at low temperature (80 K) are broad and similar to those recorded at RT. At this temperature **Cz-BzN** does not display delayed fluorescence, while the **Pht-BzN** clearly shows a relatively intense delayed component at a similar energy as TADF at RT (2.58 eV *vs.* 2.61 eV respectively). The occurrence of TADF in **Pht-BzN** at 80 K can be explained by a near zero ΔE_{ST} in this compound. **Cz-BzN** with a significantly larger ΔE_{ST} does not display TADF at this temperature but phosphorescence can be observed instead. Phosphorescence of **Cz-BzN** recorded at time delay of 70 ms is broad and featureless, with the onset red shifted in respect to the phosphorescence of pure carbazole (Fig. 9a). This behaviour of the phosphorescence spectrum is highly suggestive of a delocalized nature of the T_1 state due to partial D–A conjugation. In **Pht-BzN**, at 80 K, between 50 μs and 100 ms delay, the emission progressively blue shifts showing a subtle vibronic structure (Fig. S30, ESI†) which resembles that

of phenothiazine phosphorescence. Such behaviour indicates that the long-lived emission may be related to the ^{3}LE state localised on the donor.

Time-resolved photophysical study of bulk Cz-BzN and Pht-BzN crystals. The time-resolved behaviour of **Cz-BzN** and **Pht-BzN** crystals was studied at various temperatures. Here we present the results for **Pht-BzN** crystal at 295 K (Fig. 10a) and 80 K (Fig. 10b), while the time-resolved spectra for **Pht-BzN** crystal recorded at intermediate temperatures are presented in the ESI,† Fig. S32. The results for **Cz-BzN** crystalline powder are reported in Fig. S25a (RT) and b (ESI†) (80 K). We note that **Cz-BzN** does not show any DF at RT (Fig. S25a, ESI†). This is in line with the hypothesis that the molecules in crystal retain their S_0 geometry after excitation in crystal form. In such case, the molecules in crystal cannot relax their geometry in the excited state as they do in PMMA and in solution, where such relaxation leads to a reduction in ΔE_{ST} (see section DFT calculations above). A more detailed discussion of this aspect can be found in the ESI,† Section 3.4.2. In contrast to **Cz-BzN**, **Pht-BzN** crystals show strong TADF at RT and the time-resolved PL spectra at 295 K (Fig. 10a) are invariant with time delay. We can observe that the phosphorescence of phenothiazine is at significantly lower energy than the long-lived PL of **Pht-BzN** crystals at 80 K (Fig. 10c). Hence, it appears that the energy of the lowest triplet state (which we believe is, thus, ^{3}CT) is higher in energy than the ^{3}LE of free phenothiazine (Scheme 1).
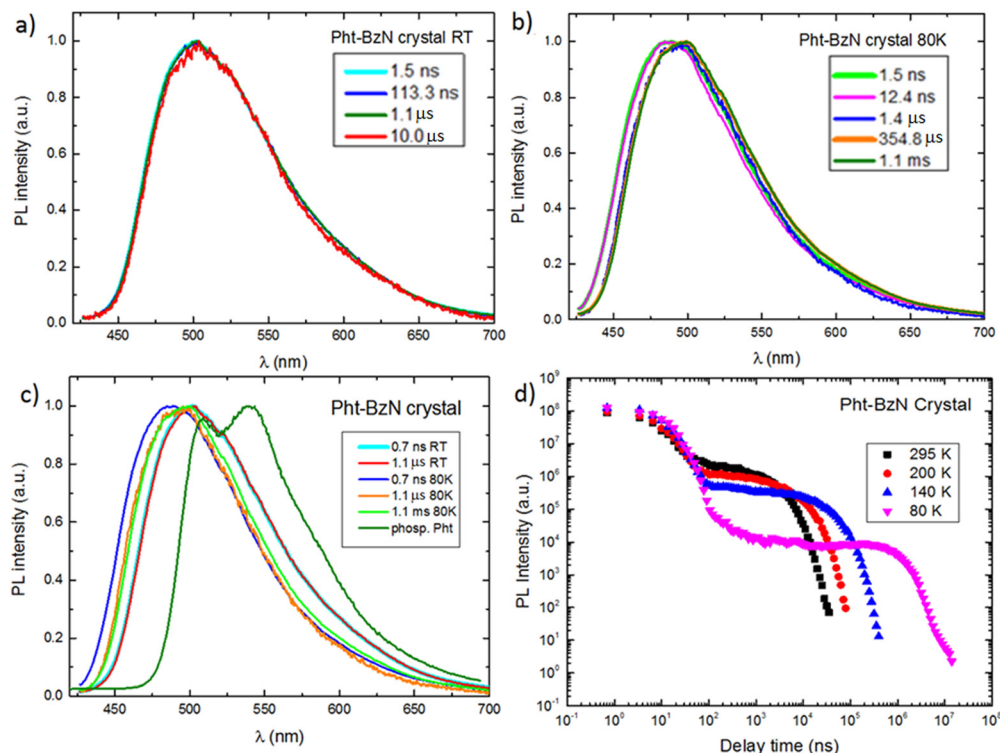
Fig. 10 Photoluminescence of **Pht-BzN** crystals: (a) time-resolved emission spectra at RT; (b) time-resolved emission spectra at 80 K; (c) time-resolved emission spectra at room temperature and 80 K in comparison with the phosphorescence spectrum of phenothiazine. (d) Decay transients at various temperatures indicated in the figure legend. λ_{ex} = 355 nm.

This behaviour indicates an apparent violation of the rule of thumb for the role of local triplet states in the TADF mechanism.[56] We believe it is likely that the ^{3}LE state of phenothiazine moiety in the crystal [denoted as ^{3}LE (Pht)$_{crystal}$, Scheme 1] might be of higher energy than in free phenothiazine [^{3}LE (Pht), Scheme 1] due to the molecule geometry being frozen at its S_0 geometry. Thus, not only the frozen ground state geometry offers oscillator strength $f > 0$ accounting for high PLQY, but also enables fine tuning of the excited state energy leading to minimal ΔE_{ST}. The condition $\Delta E_{ST} \approx 0$ is thus achieved by increasing the ^{3}LE energy of the donor upon freezing its configuration. Such behaviour demonstrates a

significant novelty over previous accounts of AIE or similar phenomena. Based on these considerations and considering that the emission spectra of **Pht-BzN** crystals at 80 K remain completely invariant of time delay from 1 μs to 1 ms (Fig. 10c) it is likely that the observed long-lived emission can be assigned to TADF rather than ^{3}CT phosphorescence.

Considering the increase of total PL intensity of **Pht-BzN** crystals at lower temperatures (Fig. 10d) we estimate that the PLQY increases to ~90% at 80 K from 39% at RT. **Pht-BzN** displays prominent TADF properties in crystal (Fig. 10d) as the DF/PF = 5 at RT is an order of magnitude larger than in PMMA (Table 3). The DF/PF ratio increases further at 80 K to 7.3 (Table 3), which is due to the suppression of non-radiative processes affecting mostly the triplet state. An increase rather than decrease of the DF/PF at 80 K is a further indication that the TADF mechanism is not significantly suppressed at this temperature, reaffirming that $\Delta E_{ST} \approx 0$.

Oxygen is known to quench long-lived PL in solution and in solid state. The decay profiles of **Pht-BzN** crystal in vacuum and in air are however almost identical (Fig. S31, ESI†). This important finding suggests that **Pht-BzN** crystals do not allow oxygen to permeate and diffuse as they are dense and display tight molecular packing. This in turn prevents quenching of long-lived excited states. Such effect is highly desirable, as it provides excellent TADF and PL characteristics of crystals without the requirement to remove oxygen or use encapsulation.

Time-resolved photophysical study of Pht-BzN microcrystals in suspension. Time-resolved photophysical properties of the
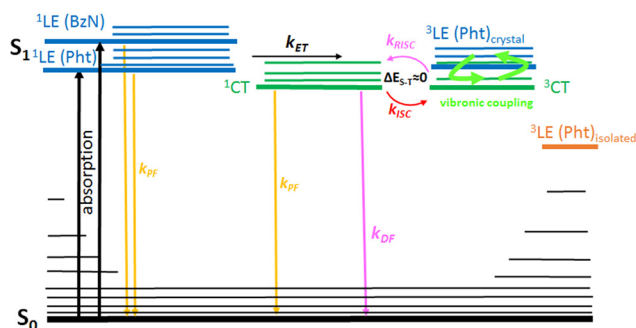
Scheme 1 Proposed energy diagram showing the electronic energy levels involved in the TADF mechanism for **Pht-BzN** in the crystalline form. We also show where phenothiazine triplet energy is expected [^{3}LE(Pht)] and where we believe it lays in the **Pht-BzN** crystal [^{3}LE(Pht)$_{crystal}$].

This journal is © The Royal Society of Chemistry 2024

J. Mater. Chem. C, 2024, **12**, 7943–7955 | **7951**
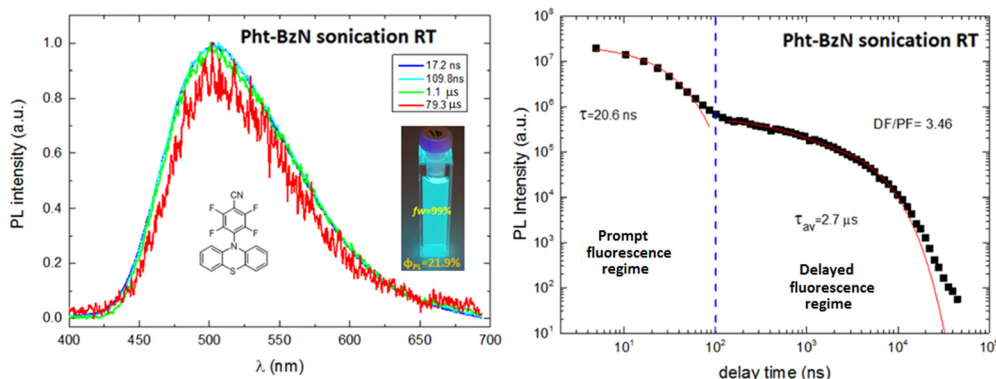
Fig. 11 Dispersion of **Pht-BzN** microcrystals in water/THF mixture (after sonication): (left) Time-resolved emission spectra at room temperature (RT); (right) photoluminescence decay trace at room temperature. λ_{ex} = 355 nm.

Pht-BzN microcrystals obtained by sonication (Fig. 11) are overall very similar to those recorded for the crystalline powder. Also in this case, the time-resolved spectra are invariant with delay time. The TADF characteristics of the dispersion are also similar to the crystalline powder, but DF/PF = 3.46 and PLQY = 21% are slightly smaller (Table 3). Inferior TADF properties and PLQY of microcrystals can be attributed to a larger surface area to volume ratio in relation to larger crystals, resulting in a stronger influence of quenchers on their PL. On the other hand, microcrystals may contain occluded contaminants due to the way they are formed, including residue of the amorphous phase or the water/THF mixture.

Comparison of photoluminescence properties between Cz-BzN, Phx-BzN, and Pht-BzN. In this section we summarize the divergent photoluminescent characteristics of the three D–A luminophores studied in this work. **Cz-BzN** shows moderate CIEE properties but no TADF in crystal. This is because the molecule in the crystal form is forced to maintain a small D–A angle similar to that of the S_0 configuration. However, in solution, or when dispersed in a polymer matrix the molecule undergoes reorganization in the excited state (at least to some extent), leading to a decrease in ΔE_{ST} and activation of TADF. **Pht-BzN** and **Phx-BzN** present a different behavior in respect to **Cz-BzN**. In solution, where the **Pht-BzN** molecule is free to relax its excited state geometry, only a negligible emission can be observed. Here, the D–A units become perfectly orthogonal, leading to a pure CT transition which is symmetry forbidden, thus oscillator strength f = 0 (Table S7, ESI†). However, in the crystal form the emission is activated because the tight packing prevents geometry relaxation to occur and the molecules remain locked in the S_0 geometry. At the S_0 geometry the D and A are near, but not perfectly orthogonal, allowing the CT transition to be luminescent with f = 0.0006 (Table S7, ESI†). **Pht-BzN** displays low luminescent properties in PMMA, yet visibly improved in respect to solutions. The more rigid environment of the PMMA polymer host prevents some non-radiative decay, but the **Pht-BzN** molecule is still able to rearrange in the excited state, thus the oscillator strength $f \approx 0$. **Phx-BzN** behaviour is somewhat similar to that of **Pht-BzN**, but less pronounced, hence in this work we focused on the latter example.

Conclusion

A series of three D–A compounds featuring a BzN electron acceptor decorated with carbazole (**Cz-BzN**), phenothiazine (**Pht-BzN**) or phenoxazine (**Phx-BzN**) donors have been investigated. In this work we have focused on **Cz-BzN** and **Pht-BzN** as the most prominent examples to demonstrate the effects of excited state geometry relaxation on photophysical properties in solution, film, and crystal. In particular, we have shown that the D–A dihedral angle increases towards full orthogonality in the excited state, while it remains smaller in the ground state. This finding has strong implications on the photoluminescent properties of crystals. **Pht-BzN** molecules, unable to relax their geometry in crystal, remain strongly emissive, but in solution or even to some extent in polymer they are allowed to relax their excited state geometry and become nearly non-emissive. We thus demonstrate that **Pht-BzN** shows crystallization-induced emission with an evident activation of TADF in crystal. We demonstrate, for the first time, that activation of TADF emission relies on the property of the crystal lattice to block the molecule relaxation and retain the near-orthogonal D–A configuration from S_0. Fixing the molecule to its ground state geometry results in the oscillator strength remaining above zero, while still allowing for a very small ΔE_{ST}. Furthermore, we observe in the **Pht-BzN** crystal that the triplet energy of phenothiazine is higher than expected for the free donor moiety, hence allowing to realize $\Delta E_{ST} \sim 0$ despite a blue shifted PL.

In this work we introduce the use of ultrasounds as a tool to obtain highly emissive TADF microcrystals from amorphous nano- and microparticles dispersed in water. Thanks to the ultrasonic vibrations, the molecules can reorganize into a crystalline form which is thermodynamically more favored than the metastable amorphous phase. We therefore consider this result as a new strategy to develop luminescent organic micro-crystalline materials. These TADF microcrystals could be used in high performance optoelectronic devices, advanced functional materials in biological sensing and imaging, AIE 'turn-on' probes, multifunctional AIE-active nano-systems, and self-assembly materials. To the best of our knowledge, this is the first time this phenomenon is demonstrated and we suggest to name it sonocrystallization-induced TADF (SCI-TADF).

7952 | *J. Mater. Chem. C,* 2024, **12**, 7943–7955

This journal is © The Royal Society of Chemistry 2024

In light of these considerations, we believe that the reported AIE and CIE properties of the presented molecules show a potential to be applied in various research areas, especially in the emergent area of bio-nanotechnology and cell bioimaging. We believe therefore that further development of both the use of sonication for obtaining luminescent microcrystals and the control of photophysical properties by using crystals and microcrystals to switch on and off TADF, will enable the development of future efficient emissive materials and could play an important role in the field of optoelectronic devices, bioimaging, and sensing.

Conflicts of interest

There are no conflicts to declare.

Acknowledgements

References

1 Q. S. Zhang, H. Kuwabara, W. J. Potscavage, S. P. Huang, Y. Hatae, T. Shibata and C. Adachi, Anthraquinone-Based Intramolecular Charge-Transfer Compounds: Computational Molecular Design, Thermally Activated Delayed Fluorescence, and Highly Efficient Red Electroluminescence, *J. Am. Chem. Soc.*, 2014, **136**(52), 18070–18081.

2 Y. Im, M. Kim, Y. J. Cho, J.-A. Seo, K. S. Yook and J. Y. Lee, Molecular Design Strategy of Organic Thermally Activated Delayed Fluorescence Emitters, *Chem. Mater.*, 2017, **29**(5), 1946–1963.

3 X. Han, Q. Bai, L. Yao, H. C. Liu, Y. Gao, J. Y. Li, L. Q. Liu, Y. L. Liu, X. X. Li, P. Lu and B. Yang, Highly Efficient Solid-State Near-Infrared Emitting Material Based on Triphenylamine and Diphenylfumaronitrile with an EQE of 2.58% in Nondoped Organic Light-Emitting Diode, *Adv. Funct. Mater.*, 2015, **25**(48), 7521–7529.

4 X. Liang, Z. L. Tu and Y. X. Zheng, Thermally Activated Delayed Fluorescence Materials: Towards Realization of High Efficiency through Strategic Small Molecular Design, *Chem. – Eur. J.*, 2019, **25**(22), 5623–5642.

5 Y. Tao, K. Yuan, T. Chen, P. Xu, H. H. Li, R. F. Chen, C. Zheng, L. Zhang and W. Huang, Thermally Activated Delayed Fluorescence Materials Towards the Breakthrough of Organoelectronics, *Adv. Mater.*, 2014, **26**(47), 7931–7958.

6 D. Song, Y. Yu, L. Yue, D. Zhong, Y. Zhang, X. Yang, Y. Sun, G. Zhou and Z. Wu, Asymmetric thermally activated delayed fluorescence (TADF) emitters with 5,9-dioxa-13*b*-boranaphtho-[3,2,1-*de*]anthracene (OBA) as the acceptor and highly efficient blue-emitting OLEDs, *J. Mater. Chem. C*, 2019, **7**(38), 11953–11963.

7 R. S. Nobuyasu, J. S. Ward, J. Gibson, B. A. Laidlaw, Z. J. Ren, P. Data, A. S. Batsanov, T. J. Penfold, M. R. Bryce and F. B. Dias, The influence of molecular geometry on the efficiency of thermally activated delayed fluorescence, *J. Mater. Chem. C*, 2019, **7**(22), 6672–6684.

8 D. Zhong, Y. Yu, D. Song, X. Yang, Y. Zhang, X. Chen, G. Zhou and Z. Wu, Organic Emitters with a Rigid 9-Phenyl-9-phosphafluorene Oxide Moiety as the Acceptor and Their Thermally Activated Delayed Fluorescence Behavior, *ACS Appl. Mater. Interfaces*, 2019, **11**(30), 27112–27124.

9 D. Zhong, Y. Yu, L. Yue, X. Yang, L. Ma, G. Zhou and Z. Wu, Optimizing molecular rigidity and thermally activated delayed fluorescence (TADF) behavior of phosphoryl center π-conjugated heterocycles-based emitters by tuning chemical features of the tether groups, *Chem. Eng. J.*, 2021, **413**, 127445.

10 J. Q. Tong, Y. J. Wang, Z. Y. Wang, J. Z. Sun and B. Z. Tang, Crystallization-Induced Emission Enhancement of a Simple Tolane-Based Mesogenic Luminogen, *J. Phys. Chem. C*, 2015, **119**(38), 21875–21881.

11 Y. Q. Dong, J. W. Y. Lam, A. J. Qin, Z. Li, J. Z. Sun, H. H. Y. Sung, I. D. Williams and B. Z. Tang, Switching the light emission of (4-biphenylyl)phenyldibenzofulvene by morphological modulation: crystallization-induced emission enhancement, *Chem. Commun.*, 2007, (1), 40–42.

12 A. Maggiore, X. F. Tan, A. Brosseau, A. Danos, F. Miomandre, A. P. Monkman, P. Audebert and G. Clavier, Novel D–A chromophores with condensed 1,2,4-triazine system simultaneously display thermally activated delayed fluorescence and crystallization-induced phosphorescence, *Phys. Chem. Chem. Phys.*, 2022, **24**(29), 17770–17781.

13 Y. N. Hong, J. W. Y. Lam and B. Z. Tang, Aggregation-induced emission, *Chem. Soc. Rev.*, 2011, **40**(11), 5361–5388.

14 Y. N. Hong, J. W. Y. Lam and B. Z. Tang, Aggregation-induced emission: phenomenon, mechanism and applications, *Chem. Commun.*, 2009, (29), 4332–4353.

15 J. D. Luo, Z. L. Xie, J. W. Y. Lam, L. Cheng, H. Y. Chen, C. F. Qiu, H. S. Kwok, X. W. Zhan, Y. Q. Liu, D. B. Zhu and B. Z. Tang, Aggregation-induced emission of 1-methyl-1,2,3,4,5-pentaphenylsilole, *Chem. Commun.*, 2001, (18), 1740–1741.

16 J. W. Chen, C. C. W. Law, J. W. Y. Lam, Y. P. Dong, S. M. F. Lo, I. D. Williams, D. B. Zhu and B. Z. Tang,

Synthesis, light emission, nanoaggregation, and restricted intramolecular rotation of 1,1-substituted 2,3,4,5-tetraphenylsiloles, *Chem. Mater.*, 2003, **15**(7), 1535–1546.

17 C. Park, J. E. Park and H. C. Choi, Crystallization-Induced Properties from Morphology-Controlled Organic Crystals, *Acc. Chem. Res.*, 2014, **47**(8), 2353–2364.

18 C. Effertz, *Organic molecular crystals: from thin-films to devices: investigation of thin-film formation and electronic transport properties of polycrystalline perylene films, Dissertation/PhD thesis*, Publikationsserver der RWTH Aachen University, 2011.

19 Y. Q. Dong, J. W. Y. Lam, A. J. Qin, J. Z. Liu, Z. Li and B. Z. Tang, Aggregation-induced emissions of tetraphenylethene derivatives and their utilities as chemical vapor sensors and in organic light-emitting diodes, *Appl. Phys. Lett.*, 2007, **91**(1), 011111.

20 A. Maggiore, M. Pugliese, F. Di Maria, G. Accorsi, M. Gazzano, E. Fabiano, V. Tasco, M. Esposito, M. Cuscuna, L. Blasi, A. Capodilupo, G. Ciccarella, G. Gigli and V. Maiorano, Exploiting Photo- and Electroluminescence Properties of FIrpic Organic Crystals, *Inorg. Chem.*, 2016, **55**(13), 6532–6538.

21 Y. Y. Yuan, S. D. Xu, C. J. Zhang, R. Y. Zhang and B. Liu, Dual-targeted activatable photosensitizers with aggregation-induced emission (AIE) characteristics for image-guided photodynamic cancer cell ablation, *J. Mater. Chem. B*, 2016, **4**(1), 169–176.

22 W. B. Wu, D. Mao, S. D. Xu, S. L. Ji, F. Hu, D. Ding, D. L. Kong and B. Liu, High performance photosensitizers with aggregation-induced emission for image-guided photodynamic anticancer therapy, *Mater. Horiz.*, 2017, **4**(6), 1110–1114.

23 J. J. Zhang, L. L. Ning, J. G. Huang, C. Zhang and K. Y. Pu, Activatable molecular agents for cancer theranostics, *Chem. Sci.*, 2020, **11**(3), 618–630.

24 W. B. Wu and Z. Li, Nanoprobes with aggregation-induced emission for theranostics, *Mater. Chem. Front.*, 2021, **5**(2), 603–626.

25 S. Samanta, U. Manna, T. Ray and G. Das, An aggregation-induced emission (AIE) active probe for multiple targets: a fluorescent sensor for Zn^{2+} and Al^{3+} & a colorimetric sensor for Cu^{2+} and F, *Dalton Trans.*, 2015, **44**(43), 18902–18910.

26 S. Dey, R. Purkait, K. Pal, K. Jana and C. Sinha, Aggregation-Induced Emission-Active Hydrazide-Based Probe: Selective Sensing of Al^{3+}, HF^{2-}, and Nitro Explosives, *ACS Omega*, 2019, **4**(5), 8451–8464.

27 M. Shellaiah and K. W. Sun, Pyrene-Based AIE Active Materials for Bioimaging and Theranostics Applications, *Biosensors*, 2022, **12**(7), 550.

28 S. K. Samanta, K. Maiti, S. K. Manna, S. S. Ali, U. N. Guria, A. Ghosh, P. Datta and A. K. Mahapatra, An aggregation-induced emission (AIE)-active fluorescent chemodosimeter for selective sensing of hypochlorite in water and solid state: Endogenous detection of hypochlorite in live cells, *Dyes Pigm.*, 2021, **196**, 109758.

29 M. Maruthi and S. K. Kalangi, Advances in aggregation induced emission (AIE) materials in biosensing and imaging of bacteria, *Prog. Mol. Biol. Transl. Sci.*, 2021, **184**, 61–79.

30 Y. L. Balachandran and X. Y. Jiang, Aggregation-Induced Fluorogens in Bio-Detection, Tumor Imaging, and Therapy: A Review, *CCS Chem.*, 2022, **4**(2), 420–436.

31 C. K. Zhang, Y. Q. Zhao, D. D. Li, J. J. Liu, H. G. Han, D. Y. He, X. H. Tian, S. L. Li, J. Y. Wu and Y. P. Tian, Aggregation-induced emission (AIE)-active molecules bearing singlet oxygen generation activities: the tunable singlet-triplet energy gap matters, *Chem. Commun.*, 2019, **55**(10), 1450–1453.

32 I. M. Khan, S. Niazi, M. K. I. Khan, I. Pasha, A. Mohsin, J. Haider, M. W. Iqbal, A. Rehman, L. Yue and Z. P. Wang, Recent advances and perspectives of aggregation-induced emission as an emerging platform for detection and bioimaging, *Trac, Trends Anal. Chem.*, 2019, **119**, 115637.

33 Y. Z. Song, B. H. Li, S. S. Liu, M. Qin, Y. Gao, K. Zhang, L. L. Lin, C. K. Wang and J. Z. Fan, Theoretical studies on the excited-state properties of thermally activated delayed fluorescence molecules with aggregation induced emission, *J. Mater. Chem. C*, 2022, **10**(24), 9377–9390.

34 H. Liu, J. J. Guo, Z. J. Zhao and B. Tang, Aggregation-Induced Delayed Fluorescence, *ChemPhotoChem*, 2019, **3**(10), 993–999.

35 R. Furue, T. Nishimoto, I. S. Park, J. Lee and T. Yasuda, Aggregation-Induced Delayed Fluorescence Based on Donor/Acceptor-Tethered Janus Carborane Triads: Unique Photophysical Properties of Nondoped OLEDs, *Angew. Chem., Int. Ed.*, 2016, **55**(25), 7171–7175.

36 H. Wang, L. S. Xie, Q. Peng, L. Q. Meng, Y. Wang, Y. P. Yi and P. F. Wang, Novel Thermally Activated Delayed Fluorescence Materials-Thioxanthone Derivatives and Their Applications for Highly Efficient OLEDs, *Adv. Mater.*, 2014, **26**(30), 5198–5204.

37 S. D. Xu, T. T. Liu, Y. X. Mu, Y. F. Wang, Z. G. Chi, C. C. Lo, S. W. Liu, Y. Zhang, A. Lien and J. R. Xu, An Organic Molecule with Asymmetric Structure Exhibiting Aggregation-Induced Emission, Delayed Fluorescence, and Mechanoluminescence, *Angew. Chem., Int. Ed.*, 2015, **54**(3), 874–878.

38 I. H. Lee, W. Song and J. Y. Lee, Aggregation-induced emission type thermally activated delayed fluorescent materials for high efficiency in non-doped organic light-emitting diodes, *Org. Electron.*, 2016, **29**, 22–26.

39 S. F. Gan, W. W. Luo, B. R. He, L. Chen, H. Nie, R. R. Hu, A. J. Qin, Z. J. Zhao and B. Z. Tang, Integration of aggregation-induced emission and delayed fluorescence into electronic donor-acceptor conjugates, *J. Mater. Chem. C*, 2016, **4**(17), 3705–3708.

40 R. Furue, T. Nishimoto, I. S. Park, J. Lee and T. Yasuda, Aggregation-Induced Delayed Fluorescence Based on Donor/Acceptor-Tethered Janus Carborane Triads: Unique Photophysical Properties of Nondoped OLEDs, *Angew. Chem., Int. Ed.*, 2016, **55**(25), 7171–7175.

41 N. Aizawa, C.-J. Tsou, I. S. Park and T. Yasuda, Aggregation-induced delayed fluorescence from phenothiazine-containing donor–acceptor molecules for high-efficiency non-doped organic light-emitting diodes, *Polym. J.*, 2017, **49**(1), 197–202.

7954 | *J. Mater. Chem. C*, 2024, **12**, 7943–7955

This journal is © The Royal Society of Chemistry 2024

42 S. P. Xiang, Z. Huang, S. Q. Sun, X. L. Lv, L. W. Fan, S. F. Ye, H. T. Chen, R. D. Guo and L. Wang, Highly efficient non-doped OLEDs using aggregation-induced delayed fluorescence materials based on 10-phenyl-10*H*-phenothiazine 5,5-dioxide derivatives, *J. Mater. Chem. C*, 2018, **6**(42), 11436–11443.

43 J. Huang, H. Nie, J. Zeng, Z. Zhuang, S. Gan, Y. Cai, J. Guo, S. J. Su, Z. Zhao and B. Z. Tang, Highly Efficient Nondoped OLEDs with Negligible Efficiency Roll-Off Fabricated from Aggregation-Induced Delayed Fluorescence Luminogens, *Angew. Chem., Int. Ed.*, 2017, **56**(42), 12971–12976.

44 J. J. Guo, J. Z. Fan, L. L. Lin, J. J. Zeng, H. Liu, C. K. Wang, Z. J. Zhao and B. Z. Tang, Mechanical Insights into Aggregation-Induced Delayed Fluorescence Materials with Anti-Kasha Behavior, *Adv. Sci.*, 2019, **6**(3), 1801629.

45 F. L. Ma, Y. Cheng, Y. Zheng, H. F. Ji, K. Hasrat and Z. J. Qi, Rational design of thermally activated delayed fluorescence emitters with aggregation-induced emission employing combined charge transfer pathways for fabricating efficient non-doped OLEDs, *J. Mater. Chem. C*, 2019, **7**(30), 9413–9422.

46 A. Maggiore, Y. Y. Qu, R. Guillot, P. Pander, M. Vasylieva, P. Data, F. B. Dias, P. Audebert, G. Clavier and F. Miomandre, Novel Easy to Synthesize Benzonitrile Compounds with Mixed Carbazole and Phenoxazine Substituents Exhibiting Dual Emission and TADF Properties, *J. Phys. Chem. B*, 2022, **126**(14), 2740–2753.

47 F. B. Dias, T. J. Penfold and A. P. Monkman, Photophysics of thermally activated delayed fluorescence molecules, *Methods Appl. Fluoresc.*, 2017, **5**(1), 012001.

48 G. R. Suman, M. Pandey and A. S. J. Chakravarthy, Review on new horizons of aggregation induced emission: from design to development, *Mater. Chem. Front.*, 2021, **5**(4), 1541–1584.

49 D. G. Rickerby and M. Morrison, Nanotechnology and the environment: A European perspective, *Sci. Technol. Adv. Mater.*, 2007, **8**(1–2), 19.

50 B. Bhushan, Introduction to nanotechnology, *Springer Handbook Nanotechnol.*, 2017, 1–19.

51 J. Schulte, *Nanotechnology: global strategies, industry trends and applications*, John Wiley & Sons, 2005.

52 I. Y. Wong, S. N. Bhatia and M. Toner, Nanotechnology: emerging tools for biology and medicine, *Genes Dev.*, 2013, **27**(22), 2397–2408.

53 S. S. Ray and J. Bandyopadhyay, Nanotechnology-enabled biomedical engineering: current trends, future scopes, and perspectives, *Nanotechnol. Rev.*, 2021, **10**(1), 728–743.

54 A. Stockmann, J. Kurzawa, N. Fritz, N. Acar, S. Schneider, J. Daub, R. Engl and T. Clark, Conformational control of photoinduced charge separation within phenothiazine-pyrene dyads, *J. Phys. Chem. A*, 2002, **106**(34), 7958–7970.

55 M. Aydemir, S. D. Xu, C. J. Chen, M. R. Bryce, Z. G. Chi and A. P. Monkman, Photophysics of an Asymmetric Donor-Acceptor-Donor' TADF Molecule and Reinterpretation of Aggregation-Induced TADF Emission in These Materials, *J. Phys. Chem. C*, 2017, **121**(33), 17764–17772.

56 F. B. Dias, J. Santos, D. R. Graves, P. Data, R. S. Nobuyasu, M. A. Fox, A. S. Batsanov, T. Palmeira, M. N. Berberan-Santos, M. R. Bryce and A. P. Monkman, The Role of Local Triplet Excited States and D–A Relative Orientation in

57 N. Siraj, S. Das, F. Hasan, C. F. Lu, L. W. Kiruri, K. E. S. Gall and I. M. Warner, Enhanced S-2 emission in carbazole-based ionic liquids, *RSC Adv.*, 2015, **5**(13), 9939–9945.

58 R.-B. Sergio MBonesi, Electronic spectroscopy of carbazole and N- and C-substituted carbazoles in homogeneous media and in solid matrix, *J. Luminescence*, 2001, **93**(1), 51–74.

59 J. A. Vanallan, R. E. Adel and G. A. Reynolds, POLYNUC-LEAR HETEROCYCLES. 1. 1H-BENZO B PYRIDOL 1,2,3-MN PHENOXAZIN-1-1 AND RELATED SUBSTANCES, *J. Org. Chem.*, 1962, **27**(5), 1659–1664.

60 W. Rettig, Photoinduced charge separation *via* twisted intramolecular charge transfer states, *Electron Transfer I. Topics in Current Chemistry*, Springer, Berlin, Heidelberg, 1994, vol. 169, pp. 253–299.

61 M. N. B.-S. Bernard Valeur, *Molecular Fluorescence: Principles and Applications*, Wiley-VCH, Weinheim, 2nd edn, 2012, p. 592.

62 C. Reichardt, SOLVATOCHROMIC DYES AS SOLVENT POLARITY INDICATORS, *Chem. Rev.*, 1994, **94**(8), 2319–2358.

63 J. Gibson, A. P. Monkman and T. J. Penfold, The Importance of Vibronic Coupling for Efficient Reverse Intersystem Crossing in Thermally Activated Delayed Fluorescence Molecules, *ChemPhysChem*, 2016, **17**(19), 2956–2961.

64 M. K. Etherington, J. Gibson, H. F. Higginbotham, T. J. Penfold and A. P. Monkman, Revealing the spin-vibronic coupling mechanism of thermally activated delayed fluorescence, *Nat. Commun.*, 2016, **7**, 13680.

65 F. B. Dias, J. Santos, D. R. Graves, P. Data, R. S. Nobuyasu, M. A. Fox, A. S. Batsanov, T. Palmeira, M. N. Berberan-Santos, M. R. Bryce and A. P. Monkman, The Role of Local Triplet Excited States and D–A Relative Orientation in Thermally Activated Delayed Fluorescence: Photophysics and Devices, *Adv. Sci.*, 2016, **3**(12), 1600080.

66 P. L. Santos, J. S. Ward, P. Data, A. S. Batsanov, M. R. Bryce, F. B. Dias and A. P. Monkman, Engineering the singlet-triplet energy splitting in a TADF molecule, *J. Mater. Chem. C*, 2016, **4**(17), 3815–3824.

67 T. Northey, J. Stacey and T. J. Penfold, The role of solid state solvation on the charge transfer state of a thermally activated delayed fluorescence emitter, *J. Mater. Chem. C*, 2017, **5**(42), 11001–11009.

68 Y. Dong, J. W. Y. Lam, Z. Li, A. Qin, H. Tong, Y. Dong, X. Feng and B. Z. Tang, Vapochromism of Hexaphenylsilole, *J. Inorg. Organomet. Polym. Mater.*, 2005, **15**(2), 287–291.

69 M. Chapran, P. Pander, M. Vasylieva, G. Wiosna-Salyga, J. Ulanski, F. B. Dias and P. Data, Realizing 20% External Quantum Efficiency in Electroluminescence with Efficient Thermally Activated Delayed Fluorescence from an Exciplex, *ACS Appl. Mater. Interfaces*, 2019, **11**(14), 13460–13471.

70 M. Chapran, I. Sahalianov, N. N. Karaush-Karmazin, G. Wiosna-Salyga, I. Glowacki, B. Luszczynska, P. Pander and G. V. Baryshnikov, Electronic Structure of Exciplexes and the Role of Local Triplet States on Efficiency of Thermally Activated Delayed Fluorescence, *ACS Appl. Electron. Mater.*, 2023, **5**(3), 1489–1501.

This journal is © The Royal Society of Chemistry 2024

J. Mater. Chem. C, 2024, **12**, 7943–7955 | **7955**